Commun. Comput. Phys.
doi: 10.4208/cicp.OA-2016-0132

Vol. **22**, No. 5, pp. 1309-1332
November 2017

Detached Eddy Simulation of Complex Separation Flows Over a Modern Fighter Model at High Angle of Attack

Yang Zhang[1,3], Laiping Zhang[1,2,*], Xin He[1,2], Xiaogang Deng[4] and Haisheng Sun[1,3]

[1] *State Key Laboratory of Aerodynamics, China Aerodynamics Research and Development Center, Mianyang, Sichuan 621000, China.*
[2] *Computational Aerodynamics Institute, China Aerodynamics Research and Development Center, Mianyang, Sichuan 621000, China.*
[3] *Low Speed Aerodynamics Institute, China Aerodynamics Research and Development Center, Mianyang Sichuan 621000, China.*
[4] *National University of Defense Technology, Changsha, Hunan 410073, China.*

Received 13 August 2016; Accepted (in revised version) 11 March 2017

Abstract. This paper presents the simulation of complex separation flows over a modern fighter model at high angle of attack by using an unstructured/hybrid grid based Detached Eddy Simulation (DES) solver with an adaptive dissipation second-order hybrid scheme. Simulation results, including the complex vortex structures, as well as vortex breakdown phenomenon and the overall aerodynamic performance, are analyzed and compared with experimental data and unsteady Reynolds-Averaged Navier-Stokes (URANS) results, which indicates that with the DES solver, clearer vortical flow structures are captured and more accurate aerodynamic coefficients are obtained. The unsteady properties of DES flow field are investigated in detail by correlation coefficient analysis, power spectral density (PSD) analysis and proper orthogonal decomposition (POD) analysis, which indicates that the spiral motion of the primary vortex on the leeward side of the aircraft model is highly nonlinear and dominates the flow field. Through the comparisons of flow topology and pressure distributions with URANS results, the reason why higher and more accurate lift can be obtained by DES is discussed. Overall, these results show the potential capability of present DES solver in industrial applications.

AMS subject classifications: 76F99, 76M12, 65L80

Key words: Detached eddy simulation, hybrid grid, adaptive dissipation, separation flow, high angle of attack.

*Corresponding author. *Email addresses:* zhangy29v@sina.com (Y. Zhang), zhanglp_cardc@126.com (L. P. Zhang), fantasy_2003_@hotmail.com (X. He), xgdeng2000@vip.sina.com (X. G. Deng), sunhaisheng@cardc.cn (H. S. Sun)

 ©2017 Global-Science Press

https://doi.org/10.4208/cicp.OA-2016-0132 Published online by Cambridge University Press

1 Introduction

For modern fighter aircrafts, delta wing, double delta wing or diamond wing are often used in order to gain larger stall angles and generate higher lift, which is conducive to enhancement of the maneuverability of fighters. These benefits are mainly due to the leading edge vortex which dominates the flow field, but the sudden occurrence of vortex breakdown will lead to a sharp decline in aircraft performance, and even endanger flight safety, thus it is very important to accurately predict the vortical flow structures over modern fighters. With the rapid development of numerical algorithm and the rapid increase in computer power, Computational Fluid Dynamics (CFD) has been playing a more and more important role in the prediction of aerodynamic characteristics of complex modern aircrafts. Compared with experiments, numerical simulations can provide richer flow field information and meanwhile there are no influencing factors such as support interference and wind tunnel wall interference in the numerical results. However, so far it is still a great challenge for CFD to accurately simulate such large-scale separation flow. One reason is that this kind of flow belongs to the complex high Reynolds number turbulence flow, which requires a better capability of the model/solver combination to resolve turbulent structures. Another reason is that the computational cost for this kind of unsteady flow is so large that the simulations are often limited by the capacity of available computing resources [1].

To further optimize the present CFD methods in predicting complex vortex flows, three key factors need to be paid more attention, i.e., the turbulence modeling approaches, numerical schemes and mesh generation. Currently, the main methods used for numerical simulation of turbulent flows include Reynolds-Averaged Navier-Stokes (RANS) methods [2], Large-Eddy Simulation (LES) [3], Direct Numerical Simulation (DNS) [4] and RANS/LES hybrid methods [5]. Taking into account comprehensively factors such as computational cost and numerical performance, RANS/LES hybrid methods are the most potential turbulence simulation approaches in complex engineering applications at current stage and in the next period of time until LES and DNS become manageable [1]. Detached Eddy Simulation (DES) [6] is one of the most popular RANS/LES hybrid methods, because its model formulation is simple and easy to implement. Although RANS/LES hybrid methods are superior to (U)RANS methods in resolving small scale turbulent structures, low dissipative schemes are still needed in the LES region, because the excessive dissipation will prevent the methods from taking full advantage of the grid provided [7]. The central schemes without numerical dissipation seem to be more suitable for LES, but lack of computational stability is a bottleneck for their industrial applications. On the other hand, the traditional upwind schemes show good computational stability and widely used in complex engineering applications, but they are commonly considered to be too dissipative for LES [8], so high-order schemes (third order and higher) are suggested to reduce the numerical dissipation. However, the computational cost is very expensive in unsteady turbulent flow simulations with high-order schemes, especially for unstructured grids. Therefore many efforts have been made,

https://doi.org/10.4208/cicp.OA-2016-0132 Published online by Cambridge University Press

for example works by Bui [9], Travin et al. [10], Xiao et al. [11] and Deng et al. [12], to reduce the numerical dissipation of traditional upwind schemes, and these efforts are mostly based on the structured CFD algorithm. For structured CFD algorithm, the data structure is simple, but the mesh generation for complex configuration is a time consuming process, because creating the block topology requires strong experience and burdensome manual work. Although the more automatic unstructured mesh (triangles in 2D and tetrahedrons in 3D) generation technique greatly reduces the difficulties in mesh generation, unstructured mesh can not ensure solution accuracy in boundary layer regions [13]. Thus, more and more attentions are paid to hybrid mesh (triangles and quadrilaterals in 2D and tetrahedrons, prisms, pyramids and hexahedra in 3D) which offers the advantages of reduced block connectivity complexity compared with structured mesh and possible higher accuracy in viscous flow calculations compared with unstructured mesh. A comparison of the suitability of different mesh types for the computation of high Reynolds number Navier-Stokes solutions has been discussed in [13], and it indicated that hybrid mesh is more suitable for industrial CFD applications, considering both the solution accuracy and grid generation efficiency. However, as mentioned before, it is very difficult for unstructured/hybrid mesh to implement high-order schemes in simulations of complex three-dimensional configurations, though there have been some corresponding high-order discretization methods such as Discontinuous Galerkin (DG) method [14], hybrid DG/Finite-Volume (DG/FV) method [15–17], Spectral Volume (SV) method [18], Spectral Difference (SD) method [19] and Correction Procedure via Reconstruction (CPR) method [20]. One of the main reasons is that in practical applications with the use of these high-order methods the computational cost is extremely high, another reason is the robustness issue for these unstructured grid-based high-order schemes. Therefore, finite-volume methods with second order upwind schemes are still the most popular approaches in industrial applications. Consequently, it is important to solve the issue of numerical dissipation in DES applications for unstructured CFD algorithm with second-order schemes. Following this idea, an improved second-order adaptive dissipation scheme for DES applications on hybrid mesh has been developed in our previous work [21] and computational results of some typical test cases [22] have shown that the new scheme can effectively control the numerical dissipation in DES, resulting in higher resolution of vortex structures.

In this paper, the second-order adaptive dissipation scheme [22] will be further applied to DES computations of a more complex modern aircraft configuration. The DES prediction results are compared with experimental data and URANS solutions, which demonstrate the suitability of this scheme for DES in complex industrial applications. This paper is organized as follows. Section 2 introduces the hybrid adaptive dissipation scheme, as well as the DES model. The numerical results, including the vortex structures, vortex breakdown phenomenon, overall aerodynamics performance, flow topology and local pressure distributions, are presented and some analyses about the unsteady flow are also given in Section 3. Finally, the concluding remarks and future work are discussed in the last section.

https://doi.org/10.4208/cicp.OA-2016-0132 Published online by Cambridge University Press

2 Numerical method

2.1 Governing equations

2.1.1 Navier-Stokes equations

The Navier-Stokes equations in integral form can be written as:

$$\frac{\partial}{\partial t}\int_{\Omega} \boldsymbol{W} d\Omega + \oint_{\partial\Omega} (\boldsymbol{F}_c - \boldsymbol{F}_v) dS = 0, \tag{2.1}$$

where Ω is the domain of interest, or control volume, bounded by a closed surface $\partial\Omega$. $\boldsymbol{W}$ is the conservation variable vector. $\boldsymbol{F}_c$ is the inviscid flux vector and $\boldsymbol{F}_v$ is the viscous flux vector.

2.1.2 Turbulence model

The two equation k-ω Shear Stress Transport model (denoted as SST-RANS) can be written as:

$$\frac{\partial k}{\partial t} + u_j \frac{\partial k}{\partial x_j} = \frac{1}{\rho} P_k - \beta^* k\omega + \frac{1}{\rho}\frac{\partial}{\partial x_j}\left[(\mu + \sigma_k \mu_t)\frac{\partial k}{\partial x_j}\right], \tag{2.2a}$$

$$\frac{\partial \omega}{\partial t} + u_j \frac{\partial \omega}{\partial x_j} = \frac{1}{\rho} P_\omega - \beta \omega^2 + \frac{1}{\rho}\frac{\partial}{\partial x_j}\left[(\mu + \sigma_\omega \mu_t)\frac{\partial \omega}{\partial x_j}\right] + 2(1-F_1)\sigma_{\omega 2}\frac{1}{\omega}\frac{\partial k}{\partial x_j}\frac{\partial \omega}{\partial x_j}, \tag{2.2b}$$

where k is the turbulent kinetic energy, ω the specific dissipation rate of turbulent frequency, μ the molecular viscosity, μ_t the turbulent eddy viscosity, ρ density. The detailed formulations of P_k, P_ω, F_1 and constants β_*, β, σ_k, σ_ω, $\sigma_{\omega 2}$, can be found in [23]. The length scale of the SST-RANS model is $l_{k-\omega} = k^{1/2}/(\beta^*\omega)$. The DES modification in the SST-RANS model is applied to the dissipation term $\beta^* k\omega$, which can be rewritten as $k^{3/2}/l_{k-\omega}$. Substituting the Improved Delayed Detached Eddy Simulation (IDDES) length scale lIDDES [24] for RANS length scale $l_{k-\omega}$, which results in:

$$\frac{\partial k}{\partial t} + u_j \frac{\partial k}{\partial x_j} = \frac{1}{\rho} P_k - \frac{k^{3/2}}{l_{\text{IDDES}}} + \frac{1}{\rho}\frac{\partial}{\partial x_j}\left[(\mu + \sigma_k \mu_t)\frac{\partial k}{\partial x_j}\right]. \tag{2.3}$$

Combining Eq. (2.3) with Eq. (2.2b) gives the SST-based IDDES model.

2.2 Spatial and temporal discretizations

Eq. (2.1) is discretized using an unstructured/hybrid grid based second order finite volume method. A piecewise linear reconstruction procedure is used and then the variables are interpolated to the central points of the faces of the control volumes. The gradients of each cell are reconstructed with the Green-Gauss method [25]. A central scheme is used for the diffusion terms. The inviscid terms are calculated using the adaptive dissipation

https://doi.org/10.4208/cicp.OA-2016-0132 Published online by Cambridge University Press

scheme in [21, 22], which is a modified Roe's flux-splitting scheme and also is a hybrid scheme. The corresponding inviscid numerical flux can be written as:

$$\boldsymbol{F}=\frac{1}{2}(\boldsymbol{F}_L+\boldsymbol{F}_R)+\sigma\left[\frac{1}{2}|\tilde{\boldsymbol{A}}|(\boldsymbol{U}_R-\boldsymbol{U}_L)\right]. \tag{2.4}$$

Here $\boldsymbol{F}_L$ and $\boldsymbol{F}_R$ are the left and the right interpolation numerical fluxes of an interface, respectively. σ is the blending function [10] and also is the dissipation adjusting function. The value of σ ranges between 0 and 1. If $\sigma=0$, the central scheme can be obtained. If $\sigma=1$, the upwind scheme can be obtained. The dissipation level of the numerical scheme will be reduced with decreasing of σ. More details of σ can be found in [10,11,21,22], and will not be repeated here. $\tilde{\boldsymbol{A}}$ is the Roe's matrix [26]. $\boldsymbol{U}_L$ and $\boldsymbol{U}_R$ denote the left and the right interpolation variables, respectively.

A second-order backward difference scheme is adopted for time discretization. The details of the time-marching method can be found in [27].

All these modules are integrated into our compressible flow solver HyperFLOW, and the variables are stored at the cell centers. More details can refer to our previous papers [28, 29].

In Eq. (2.4), there is one point that needs to explain more, that is, the interpolating approach for central scheme and the interpolating approach for upwind scheme are the same, so the formulation of the central scheme which corresponds to the second order upwind scheme is different from that of the traditional central scheme. To make a further explanation, take the spatial discretization of the one dimensional scalar linear hyperbolic equation as an example, which can be written as:

$$\frac{\partial u}{\partial t}+a\frac{\partial u}{\partial x}=0, \tag{2.5}$$

where $a>0$ is a constant speed. A semi-discrete finite-volume approximation of Eq. (2.5) can be written as:

$$\frac{d\bar{U}_j}{dt}+\frac{a}{h}\sum_l c_l\bar{U}_{j+l}=0, \tag{2.6}$$

where $\bar{U}_j$ is the cell-averaged value, the values of l depend on the specific scheme adopted in the computation, h is the grid spacing.

In this one dimensional linear case, the upwind scheme used for DES can be reduced and written as:

$$U_f=U_{fl}=\bar{U}_j+\frac{\left(\frac{\bar{U}_{j+1}+\bar{U}_j}{2}-\frac{\bar{U}_j+\bar{U}_{j-1}}{2}\right)}{h}\times\frac{h}{2}, \tag{2.7a}$$

$$\sum_l c_l\bar{U}_{j+l}=\frac{\bar{U}_{j+1}+3\bar{U}_j-5\bar{U}_{j-1}+\bar{U}_{j-2}}{4}. \tag{2.7b}$$

https://doi.org/10.4208/cicp.OA-2016-0132 Published online by Cambridge University Press

Meanwhile, the second order central scheme with the same interpolating approach can be written as:

$$U_{fl}=\bar{U}_j+\frac{\left(\frac{\bar{U}_{j+1}+\bar{U}_j}{2}-\frac{\bar{U}_j+\bar{U}_{j-1}}{2}\right)}{h}\times\frac{h}{2}, \tag{2.8a}$$

$$U_{fr}=\bar{U}_{j+1}-\frac{\left(\frac{\bar{U}_{j+2}+\bar{U}_{j+1}}{2}-\frac{\bar{U}_{j+1}+\bar{U}_j}{2}\right)}{h}\times\frac{h}{2}, \tag{2.8b}$$

$$U_f=\frac{U_{fl}+U_{fr}}{2},\quad \sum_l c_l\bar{U}_{j+l}=\frac{-\bar{U}_{j+2}+6\bar{U}_{j+1}-6\bar{U}_{j-1}+\bar{U}_{j-2}}{8}. \tag{2.8c}$$

Blending the upwind scheme and the central scheme with the use of the dissipation adjusting function σ gives the hybrid scheme, which can be written as:

$$\sum_l c_l\bar{U}_{j+l}=\frac{-\bar{U}_{j+2}+6\bar{U}_{j+1}-6\bar{U}_{j-1}+\bar{U}_{j-2}}{8}+\sigma\frac{\bar{U}_{j+2}-4\bar{U}_{j+1}+6\bar{U}_j-4\bar{U}_{j-1}+\bar{U}_{j-2}}{8}, \tag{2.9}$$

while the traditional central scheme can be written as:

$$U_f=U_{fl}=\bar{U}_j+\frac{(\bar{U}_{j+1}-\bar{U}_j)}{h}\times\frac{h}{2}, \tag{2.10a}$$

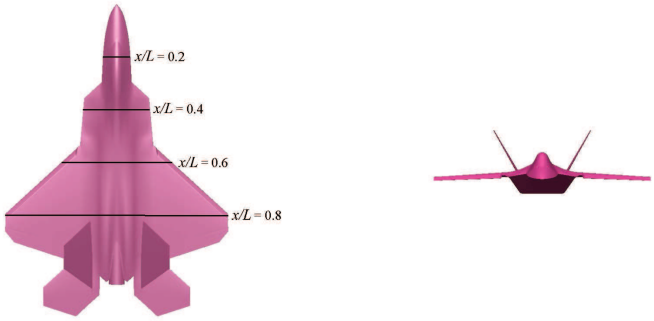
$$\sum_l c_l\bar{U}_{j+l}=\frac{\bar{U}_{j+1}-\bar{U}_{j-1}}{2}, \tag{2.10b}$$

Eqs. (2.8) and (2.10) clearly show that the stencils of the two central schemes are different, and the Fourier error analysis in [22] had indicated that the dispersive characteristic of the central scheme in Eq. (2.8) is much better than that of the traditional central scheme in Eq. (2.10), and it is even close to the dispersive characteristic of the fifth-order upwind scheme in most of the wave number range. Eq. (2.9) indicates that with decreasing of σ, the dispersive characteristic of hybrid scheme will keep the same with the central scheme in Eq. (2.8) and the dissipation level of hybrid scheme will be decreased. Thus a good performance in DES applications can be expected with this hybrid scheme.

3 Numerical results and discussions

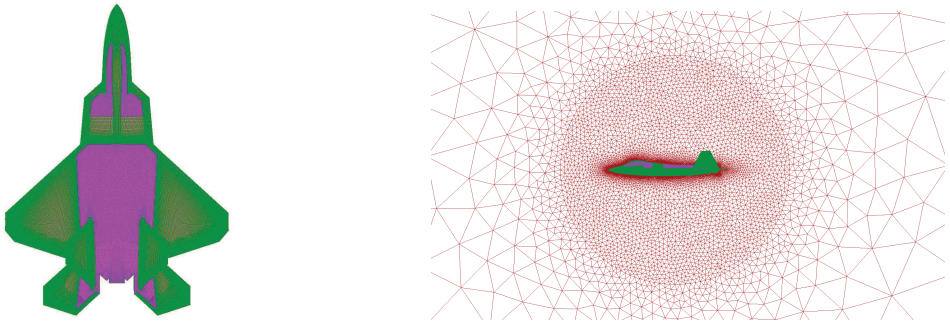
In this section, a model with modern fighter configuration is chosen for the applications, as shown in Fig. 1. The computational grid is generated by using a combination of prisms, hexahedra, pyramids and tetrahedrons. The total number of elements is about 29 million and the total number of grid points is about 12.5 million. Both prisms (the purple area in Fig. 2(a)) and hexahedra (the green area in Fig. 2(a)) are adopted near boundary layer region. Because the block topology of structured grid is too complex for the fighter configuration, prisms are used to connect some of these blocks, and then the difficulty of

https://doi.org/10.4208/cicp.OA-2016-0132 Published online by Cambridge University Press



(a) (b)

Figure 1: The modern fighter model.



(a) (b)

Figure 2: Grid topology for the fighter model: (a) Upper surface grid, (b) Symmetry plane of the hybrid grid.

mesh generation can be reduced. On the other hand, it is not easy to generate high quality mesh with semi-structured prismatic elements in some irregular areas (for example, the leading and the trailing edges of the wings), so the grid near boundary layer region is not generated by pure prismatic elements. The remaining space is filled with tetrahedral elements for simplicity (Fig. 2(b)). Some pyramids are used for the transition between hexahedral and tetrahedral elements. Fig. 3 shows the volume grid at four cross sections (as shown in Fig. 1(a), $x/L=0.2,0.4,0.6,0.8$, where x is the longitudinal coordinate and L is length of the aircraft model), which indicates that the grid spacing in the leeward is a little coarse, but considering that the computational cost has been fairly high on this hybrid grid, so the grid was not refined further. All calculations have been carried out at Mach number 0.1 and Reynolds number $Re_L=1.6\times10^6$. A non-dimensional time step of $\Delta t=0.0025L/U_\infty$ is used, where U_∞ is the free-stream velocity. The angle of attack ranges from 0° to 80°. For a complete separated case (about 17,000 non-dimensional time steps) the wall time is about 60 days with 128 Intel Central Process Unit (CPU) cores.

Fig. 4 shows the time-averaged lift, drag and pitching moment coefficients over a wide range of incidences by the SST-IDDES solver, and compares them with those of SST-

https://doi.org/10.4208/cicp.OA-2016-0132 Published online by Cambridge University Press

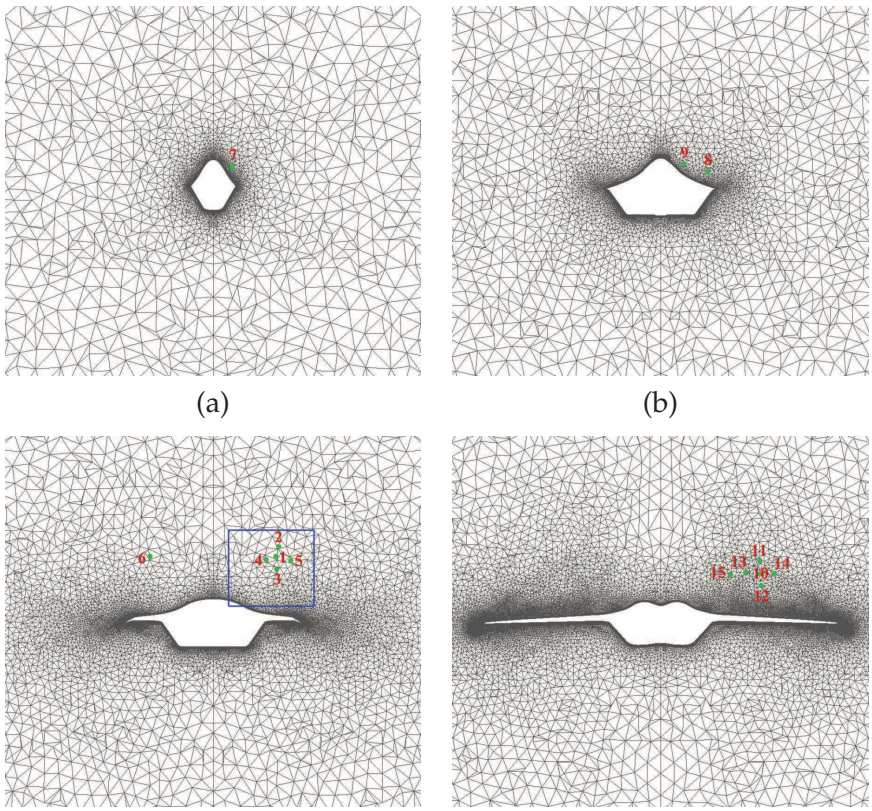


Figure 3: Cross-sections of the volume grid and locations of sampling points (a) $x/L=0.2$, (b) $x/L=0.4$, (c) $x/L=0.6$, (d) $x/L=0.8$.

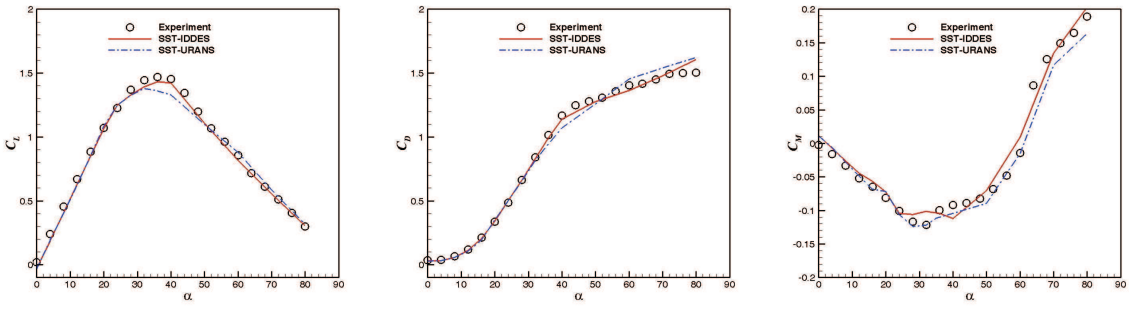


Figure 4: Comparison of IDDES and (U)RANS predictions with the experimental data (a) Lift coefficients, (b) Drag coefficients, (c) Pitching moment coefficients.

https://doi.org/10.4208/cicp.OA-2016-0132 Published online by Cambridge University Press

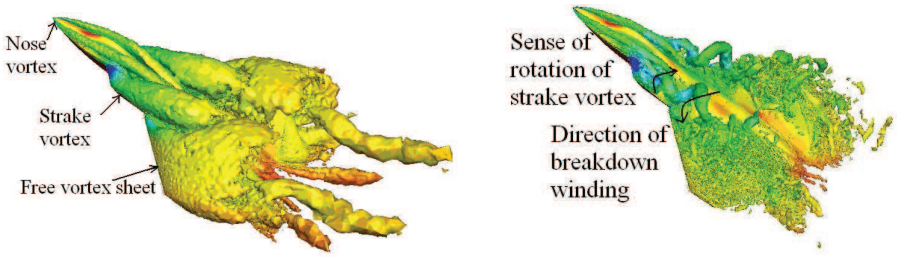


Figure 5: Iso-surfaces of Q-criterion over the fighter model at $\alpha = 36°$, (a) SST-URANS ($Q = 15$), (b) SST-IDDES-Hybrid ($Q = 300$).

URANS solver and the experimental data [30]. The IDDES results are generally in good agreement with experimental data, taking into account that there are some uncertainties in experimental data, such as support interference and wind tunnel wall interference. Differences between the two numerical results (SST-URANS and SST-IDDES) become noticeable after incidence of $\alpha = 28°$ (one of the possible reason is that at low angle of attack the flows are attached or shallowly separated, for which reasonable results also can be obtained by (U)RANS predictions), and both the stall angle of attack and maximum lift coefficient are under-predicted with SST-URANS model. To further show the superiority of SST-IDDES to SST-URANS in stall prediction, more detailed comparisons of flow fields near the stall angle are provided in the following context.

Fig. 5 shows the flow structures on the leeward side of the aircraft model in the form of instantaneous iso-surface of Q criterion (Q=300 for IDDES solutions and a lower value of $Q = 15$ for URANS solutions to visualize the flow structure more clearly) colored by pressure at $\alpha = 36°$, which is near the stall angle of attack. For SST-URANS simulation (Fig. 5(a)), although the numerical solution has captured the typical flow structures such as nose vortex (the formation of nose vortex is related to the sharp edge of the fuselage), strake vortex, and the free vortex sheet, only the large-scale vortex structures are resolved, vortex breakdown phenomenon can not be observed, and vortical flows are almost steady, which is inconsistent with the unsteady nature of the vortex-dominated flow field. On the contrary, for SST-IDDES simulation (Fig. 5(b)), not only the typical flow structures have been captured, but also the small scale turbulence flow structures are captured, which are fundamentally different from the URANS result. The free vortex sheet contains many small-scale vortices, which reflects the three-dimensional characteristics of the shear layer. For strake vortex, it can be found that the vortex core rotates around the axis of the structure, eventually disintegrates into small fragments in downstream region, and these small fragments hit the vertical tail continually. The interaction of small fragments with vertical tail surfaces is the main cause of structural vibrations and mechanical fatigue occurring in vertical tails. It also can be found that the sense of the spiral breakdown winding is opposite to the direction of rotation of the vortex itself, which is consistent with the counter-rotating phenomenon observed in other experiments [31].

https://doi.org/10.4208/cicp.OA-2016-0132 Published online by Cambridge University Press

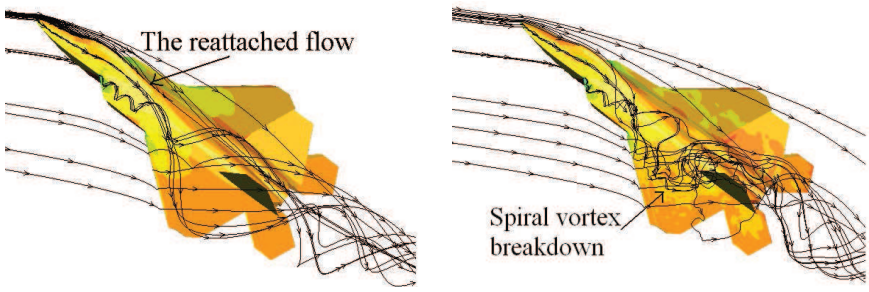


Figure 6: Streamlines of the flow field at $\alpha=36^\circ$, (a) SST-URANS, (b) SST-IDDES-Hybrid.

Fig. 6 shows the streamlines of the corresponding instantaneous numerical flow field at $\alpha=36^\circ$. Part of the incoming flow near the symmetry plane separates from the nose and then reattaches on the upper surface of the wing. The flow passing the core region of nose vortex is entrained by the strake vortex, and shifted towards the outboard of the fuselage, meanwhile the flow in the core region of nose vortex is entrained by the strake vortex in the opposite direction, and shifted towards the inboard of the fuselage. The incoming flow directly in front of the wing crosses over the upper surface of the wing, which is related to the free vortex sheet motion. The superiority of SST-IDDES solution in predicting vortex breakdown also is clearly demonstrated by the streamlines. For the SST-URANS solution, it can be observed that the streamlines passing the core region of strake vortex rotate around the vortex axis, but this motion attenuate gradually toward downstream direction, which is consistent with the phenomenon without vortex breakdown observed in Fig. 5(a). For the SST-IDDES solution, it can be observed that the winding of the corresponding streamlines increases abruptly somewhere downstream, the vortex flow suddenly becomes disordered, which reflects the characteristics of spiral vortex breakdown (the most common type of vortex breakdown over a delta wing), and the disordered flow passes the vertical tail, which corresponds to the interaction of small fragments with vertical tail surface as shown in Fig. 5(b).

To further study the unsteady vortex motion, the correlation coefficients on velocity at $\alpha=36^\circ$ are discussed. The discussion is carried out only on IDDES solution, because the URANS solution is almost steady. The definitions of correlation coefficients can be written as:

$$f(i,j)=\frac{\overline{u'(i)u'(j)}}{\sigma_u(i)\sigma_u(j)},\qquad \sigma_u(i)=\sqrt{\overline{u'(i)u'(i)}},\qquad \sigma_u(j)=\sqrt{\overline{u'(j)u'(j)}},\tag{3.1a}$$

$$g(i,j)=\frac{\overline{v'(i)v'(j)}}{\sigma_v(i)\sigma_v(j)},\qquad \sigma_v(i)=\sqrt{\overline{v'(i)v'(i)}},\qquad \sigma_v(j)=\sqrt{\overline{v'(j)v'(j)}},\tag{3.1b}$$

$$h(i,j)=\frac{\overline{w'(i)w'(j)}}{\sigma_w(i)\sigma_w(j)},\qquad \sigma_w(i)=\sqrt{\overline{w'(i)w'(i)}},\qquad \sigma_w(j)=\sqrt{\overline{w'(j)w'(j)}},\tag{3.1c}$$

https://doi.org/10.4208/cicp.OA-2016-0132 Published online by Cambridge University Press

Table 1: Coordinates of sampling points.

Number	x	y	z
1	0.60183	0.14968	0.14485
2	0.59503	0.17193	0.15116
3	0.60580	0.12015	0.14740
4	0.59924	0.14236	0.12272
5	0.60045	0.14018	0.17960
6	0.60183	0.14968	-0.14485
7	0.19887	0.05442	0.04440
8	0.40120	0.04284	0.10850
9	0.40019	0.06072	0.05553
10	0.79878	0.10951	0.22793
11	0.79934	0.14004	0.22784
12	0.79866	0.08222	0.23131
13	0.79844	0.11253	0.19576
14	0.80015	0.11043	0.26174
15	0.80132	0.10783	0.16049

where f, g, h denote respectively correlation coefficients on velocities in x, y, z directions, u, v, w denote respectively fluctuations of velocity components u, v, w, the overhead symbol "—"represents the time-averaged value, and i, j represent numbers of sampling points. Because the data set of the correlation coefficients will rise dramatically as the sampling point number increases, only a few points near vortex core regions which may be more representative are chosen for sampling. The locations of these points are shown in Fig. 3, and their coordinates are listed in Table 1. These sampling points are not accurately in cross-section planes, because the grid cells arranged irregularly. Points 1, 2, 3, 4 and 5 are located in the vortex region close to cross-section $x/L = 0.6$. Point 6 is the mirror point of point 1. Point 7 is located in the vortex region close to cross-section $x/L = 0.2$. Point 8 is located in the strake vortex region close to cross-section $x/L = 0.4$. Point 9 is located in the nose vortex region close to cross-section $x/L = 0.4$. Points 10, 11, 12, 13, 14 and 15 are located near cross-section $x/L = 0.8$, where the vortex motion is very complex and the primary vortex core is not clearly visible. As shown in Tables 2-4, the values of correlation coefficients between points at different cross-sections are very low, but this should not lead to a conclusion that there is no interaction between vortex structures at different sections, because the correlation coefficients can only reflect the linear relations. Conversely, it reflects that the motion of the primary vortex in axial direction is highly nonlinear. Meanwhile, the values of correlation coefficients between points at the same cross-sections are relatively high, and the values of correlation coefficients between points 1, 2, 3, 4 and 5 are higher than those between points 10, 11, 12, 13, 14 and 15, which indicates that the large scale vortical structures break into small scale ones, and consequently, the nonlinearity of the flow field increases. The values of correlation coefficients

https://doi.org/10.4208/cicp.OA-2016-0132 Published online by Cambridge University Press

Table 2: Correlation coefficients on u velocity component in x direction at $\alpha=36^\circ$.

$f(i,j)$	1	2	3	4	5	6	7	8	9	10	11	12	13	14	15
1	1.00	0.50	0.59	0.81	0.59	-0.09	0.31	0.07	0.09	0.07	0.04	0.12	0.09	0.04	0.16
2	0.50	1.00	-0.12	0.44	0.57	0.04	0.41	-0.07	0.15	0.11	0.08	0.07	-0.07	0.01	0.00
3	0.59	-0.12	1.00	0.45	0.18	-0.10	0.06	0.10	0.04	-0.02	-0.01	0.08	0.16	0.00	0.10
4	0.81	0.44	0.45	1.00	0.52	-0.17	0.36	0.09	0.13	0.08	0.06	0.15	0.04	0.01	0.09
5	0.59	0.57	0.18	0.52	1.00	-0.13	0.17	0.00	0.06	0.16	0.11	0.13	0.00	-0.06	0.15
6	-0.09	0.04	-0.10	-0.17	-0.13	1.00	0.04	-0.06	-0.04	-0.04	0.02	-0.09	-0.04	0.06	-0.12
7	0.31	0.41	0.06	0.36	0.17	0.04	1.00	0.03	0.31	0.06	0.10	0.20	-0.14	0.14	-0.25
8	0.07	-0.07	0.10	0.09	0.00	-0.06	0.03	1.00	-0.03	0.09	0.08	0.01	0.01	0.04	0.00
9	0.09	0.15	0.04	0.13	0.06	-0.04	0.31	-0.03	1.00	0.16	0.10	0.13	-0.04	0.16	-0.11
10	0.07	0.11	-0.02	0.08	0.16	-0.04	0.06	0.09	0.16	1.00	0.28	0.34	0.08	0.14	0.01
11	0.04	0.08	-0.01	0.06	0.11	0.02	0.10	0.08	0.10	0.28	1.00	0.04	-0.16	0.25	0.06
12	0.12	0.07	0.08	0.15	0.13	-0.09	0.20	0.01	0.13	0.34	0.04	1.00	0.08	0.06	0.01
13	0.09	-0.07	0.16	0.04	0.00	-0.04	-0.14	0.01	-0.04	0.08	-0.16	0.08	1.00	-0.17	0.18
14	0.04	0.01	0.00	0.01	-0.06	0.06	0.14	0.04	0.16	0.14	0.25	0.06	-0.17	1.00	-0.08
15	0.16	0.00	0.10	0.09	0.15	-0.12	-0.25	0.00	-0.11	0.01	0.06	0.01	0.18	-0.08	1.00

Table 3: Correlation coefficients on v velocity component in y direction at $\alpha=36^\circ$.

$g(i,j)$	1	2	3	4	5	6	7	8	9	10	11	12	13	14	15
1	1.00	0.81	0.81	0.89	0.47	-0.14	-0.14	0.07	-0.22	0.12	0.22	0.08	0.22	-0.08	-0.06
2	0.81	1.00	0.56	0.73	0.64	-0.12	-0.24	0.00	-0.19	0.07	0.17	0.09	0.14	-0.07	0.02
3	0.81	0.56	1.00	0.722	0.37	-0.10	-0.09	0.08	-0.16	0.07	0.19	-0.02	0.15	-0.02	-0.12
4	0.89	0.73	0.72	1.00	0.29	-0.16	-0.09	0.06	-0.17	0.07	0.15	0.07	0.19	-0.06	-0.14
5	0.47	0.64	0.37	0.29	1.00	-0.04	-0.21	0.05	-0.18	0.07	0.09	0.06	0.06	-0.06	0.02
6	-0.14	-0.12	-0.10	-0.16	-0.04	1.00	0.08	0.05	0.03	-0.02	0.01	0.06	-0.04	0.11	-0.05
7	-0.14	-0.24	-0.09	-0.09	-0.21	0.08	1.00	-0.03	0.39	-0.17	-0.14	-0.20	-0.18	-0.18	-0.11
8	0.07	0.00	0.08	0.06	0.05	0.05	-0.03	1.00	-0.15	0.01	0.00	0.10	0.00	0.04	-0.03
9	-0.22	-0.19	-0.16	-0.17	-0.18	0.03	0.39	-0.15	1.00	-0.14	-0.10	-0.20	-0.20	-0.07	-0.23
10	0.12	0.07	0.07	0.07	0.07	-0.02	-0.17	0.01	-0.14	1.00	0.56	0.59	0.47	0.24	0.10
11	0.22	0.17	0.19	0.15	0.09	0.01	-0.14	0.00	-0.10	0.56	1.00	0.19	0.40	0.23	0.18
12	0.08	0.09	-0.02	0.07	0.06	0.06	-0.20	0.10	-0.20	0.59	0.19	1.00	0.38	0.19	0.02
13	0.22	0.14	0.15	0.19	0.06	-0.04	-0.18	0.00	-0.20	0.47	0.40	0.38	1.00	0.06	0.22
14	-0.08	-0.07	-0.02	-0.06	-0.06	0.11	-0.18	0.04	-0.07	0.24	0.23	0.19	0.06	1.00	-0.09
15	-0.06	0.02	-0.12	-0.14	0.02	-0.05	-0.11	-0.03	-0.23	0.10	0.18	0.02	0.22	-0.09	1.00

between mirror points 1 and 6 are low, which indicates that the instantaneous flow field is not mirrored about the symmetry plane.

Fig. 7 gives the power spectral density (PSD) of pressure coefficients on the above sampling points at $\alpha=36^\circ$, and the Strouhal number (St) (or non-dimensional frequency) is defined as f_L/U_∞, where f is frequency. The PSD on point 7 is very low, which indicates that the amplitude of the pressure fluctuation is very small, and combined with Fig. 5(b), it can be inferred that the nose vortex near the cross-section $x/L=0.2$ is almost steady. The PSD on point 9 is low too, and decreases quickly as the frequency increasing. Combined with Fig. 5(b), it can be inferred that the nose vortex motion near the cross-section $x/L=0.4$ is still small. Meanwhile the unsteady pressure signal at point 8 becomes strong, the primary frequency is visible, and combined with Fig. 5(b), it can

https://doi.org/10.4208/cicp.OA-2016-0132 Published online by Cambridge University Press

Table 4: Correlation coefficients on w velocity component in z direction at $\alpha=36^\circ$.

$h(i,j)$	1	2	3	4	5	6	7	8	9	10	11	12	13	14	15
1	1.00	0.71	0.54	0.66	0.83	0.09	0.22	0.07	-0.04	-0.12	-0.11	-0.02	-0.08	-0.14	-0.05
2	0.71	1.00	0.04	0.14	0.79	-0.02	0.24	0.11	0.03	-0.16	-0.16	-0.05	-0.09	-0.11	-0.15
3	0.54	0.04	1.00	0.79	0.45	0.13	0.03	-0.05	-0.07	0.10	0.07	0.06	0.02	0.02	0.15
4	0.66	0.14	0.79	1.00	0.47	0.18	0.18	0.00	-0.01	0.06	0.05	0.06	0.01	0.01	0.10
5	0.83	0.79	0.45	0.47	1.00	0.07	0.10	0.02	0.01	-0.09	-0.06	-0.02	-0.02	-0.13	-0.07
6	0.09	-0.02	0.13	0.18	0.07	1.00	-0.06	-0.02	-0.12	-0.10	0.08	0.04	-0.05	-0.07	0.09
7	0.22	0.24	0.03	0.18	0.10	-0.06	1.00	0.08	0.11	-0.10	-0.12	-0.09	-0.13	-0.07	-0.18
8	0.07	0.11	-0.05	0.00	0.02	-0.02	0.08	1.00	-0.01	-0.09	-0.05	-0.05	-0.01	0.02	0.01
9	-0.04	0.03	-0.07	-0.01	0.01	-0.12	0.11	-0.01	1.00	0.08	-0.09	0.07	0.08	-0.09	-0.03
10	-0.12	-0.16	0.10	0.06	-0.09	-0.10	-0.10	-0.09	0.08	1.00	0.30	0.24	0.47	0.42	0.35
11	-0.11	-0.16	0.07	0.05	-0.06	0.08	-0.12	-0.05	-0.09	0.30	1.00	0.01	0.12	0.30	0.03
12	-0.02	-0.05	0.06	0.06	-0.02	0.04	-0.09	-0.05	0.07	0.24	0.01	1.00	0.17	0.10	0.31
13	-0.08	-0.09	0.02	0.01	-0.02	-0.05	-0.13	-0.01	0.08	0.47	0.12	0.17	1.00	0.12	0.53
14	-0.14	-0.11	0.02	0.01	-0.13	-0.07	-0.07	0.02	-0.09	0.42	0.30	0.10	0.12	1.00	0.18
15	-0.05	-0.15	0.15	0.10	-0.07	0.09	-0.18	0.01	-0.03	0.35	0.03	0.31	0.53	0.18	1.00

be inferred that this frequency is corresponding to the spiral rotation of the vortex core near the cross-section $x/L=0.4$. For sampling points near the cross-section $x/L=0.6$, all results show strong peaks at the same St of about 2.49. This indicates that the spiral motion of the vortex core is the main cause of pressure fluctuations near this region, and meanwhile it can be found that the PSD distributions on point 6 and point 1 are similar, so it can be inferred that the possible reason of flow field asymmetry is due to the phase difference between the two vortex motions. However, the time-averaged flow field is almost mirrored (it will be shown later in Fig. 13). For sampling points near the cross-section $x/L=0.8$, obvious primary frequencies can not be observed, which indicates that the primary vortex is totally breakdown.

The proper orthogonal decomposition (POD) method [32] is adopted to further analyze the coherent structure of the pressure field at $\alpha=36^\circ$. When implementing this method, the number of sampling points and the time steps are limited to 2102 and 3000, respectively, since a large amount of computer memory is required to calculate the POD modes. The domain chosen for visualization is a rectangular area which is shown in Fig. 3(c) (the inner region of the blue box). Fig. 8 and Fig. 9 show the time history and PSD distributions of the first four POD coefficients. The POD coefficients for modes 1 and 2 change quasi-periodically, but there is a phase difference of about $\pi/2$ between these two coefficients (Fig. 8(a)), the amplitudes of PSD at the corresponding primary frequencies are high and both primary frequencies are close to the primary frequency of the pressure fluctuation near this region, so modes 1 and 2 can be considered as a pair of modes. The variations of POD coefficients for modes 3 and 4 are more complex, the coefficient fluctuations are smaller, their corresponding PSD distributions are similar, the primary frequencies are higher relatively (Fig. 9(b)) and the amplitudes of PSD at the primary frequencies are lower, so modes 3 and 4 can be considered as another pair of modes.

https://doi.org/10.4208/cicp.OA-2016-0132 Published online by Cambridge University Press

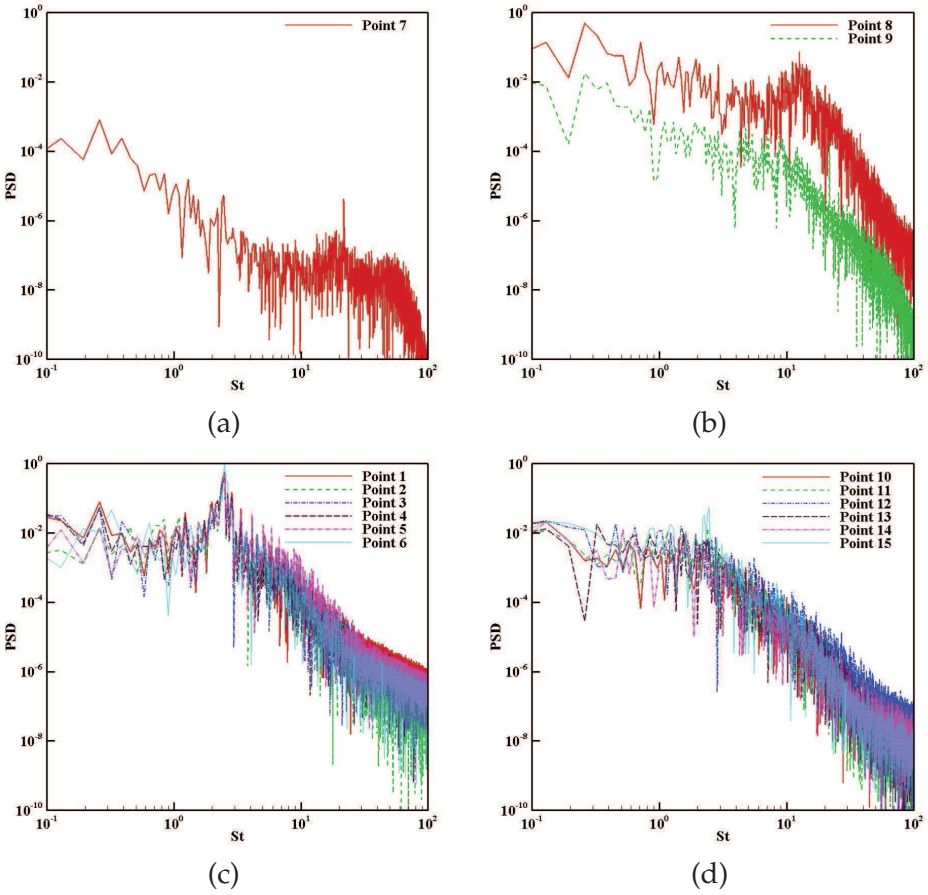


Figure 7: Power spectral density of pressure coefficients at $\alpha=36^{\circ}$, (a) Close to $x/L=0.2$, (b) Close to $x/L=0.4$, (c) Close to $x/L=0.6$, (d) Close to $x/L=0.8$.

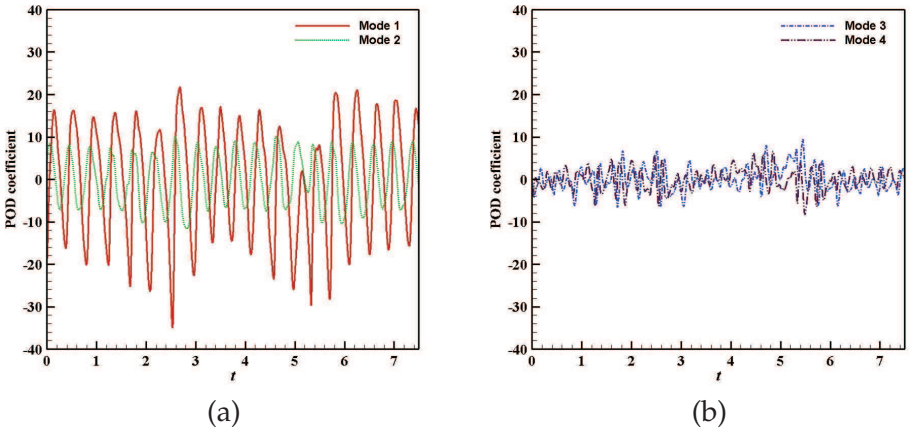


Figure 8: Time history of first four POD coefficients (a) Mode 1 and mode 2, (b) Mode 3 and mode 4.

https://doi.org/10.4208/cicp.OA-2016-0132 Published online by Cambridge University Press

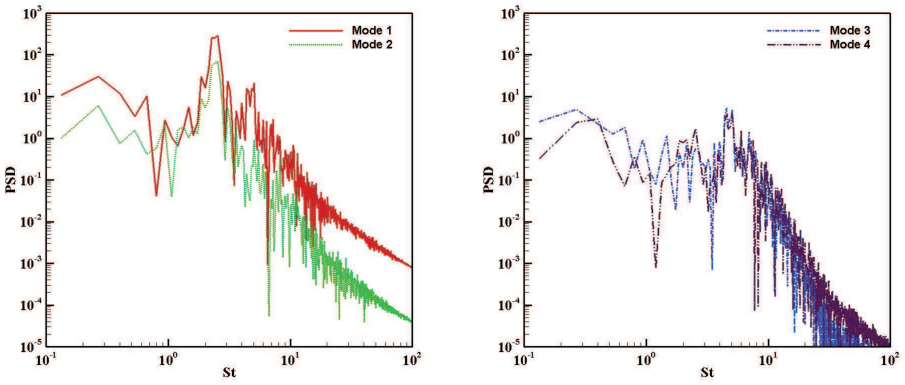


Figure 9: Power spectral density of first four POD coefficients (a) Mode 1 and mode 2, (b) Mode 3 and mode 4.

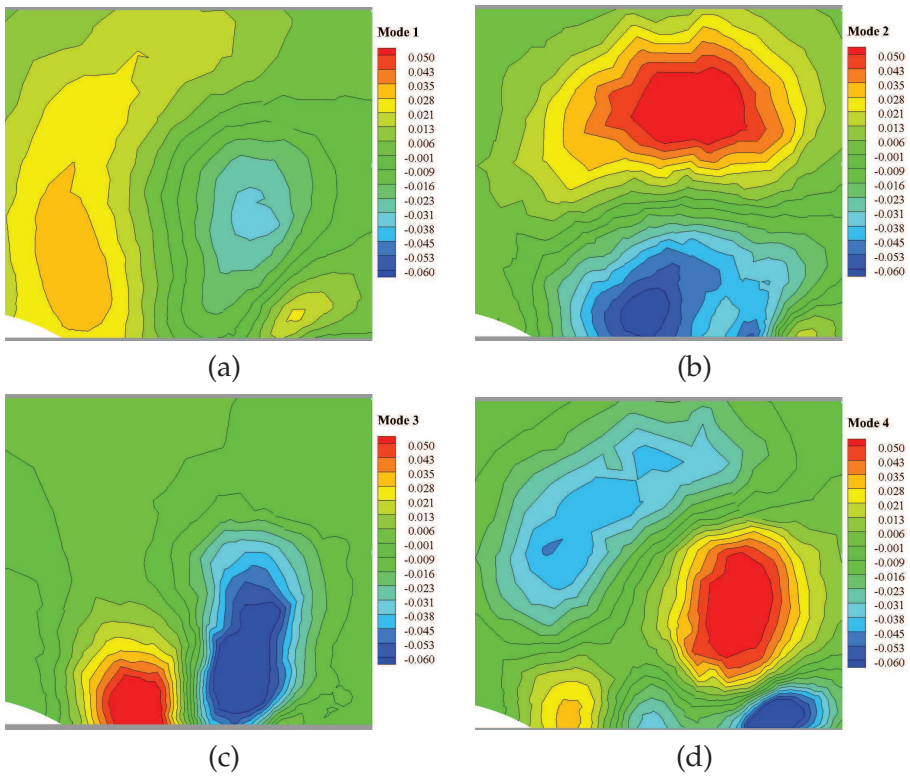
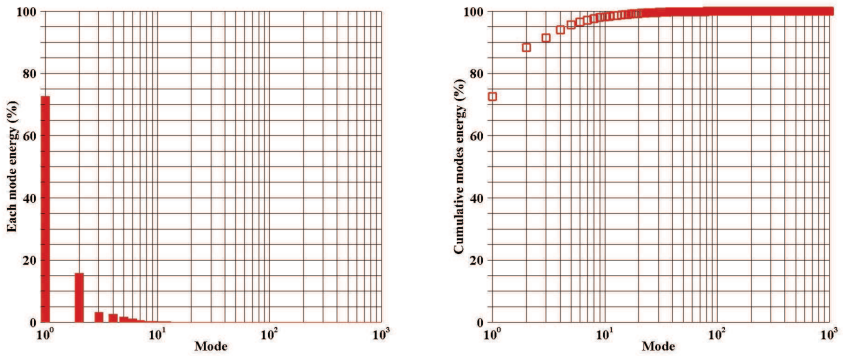


Figure 10: The first four POD modes (a) Mode 1, (b) Mode 2, (c) Mode 3, (d) Mode 4.

Fig. 10 shows the first four POD mode distributions. It can be observed that the maximum and minimum values of modes 1 and 2 are alternatively distributed. Considering that there is a phase difference of about $\pi/2$ between the two POD coefficients, the effect

https://doi.org/10.4208/cicp.OA-2016-0132 Published online by Cambridge University Press



(a) (b)

Figure 11: Energy distribution of POD modes, (a) Percentage of each POD mode energy to the total mode energy, (b) Percentage of the cumulative POD mode energy to the total mode energy.

of this pair of modes will form a rotating disturbance, which will pass the four extreme value regions in turn. Combining the PSD analysis, it is obvious that this rotating disturbance reflects the spiral rotation of the primary vortex (Fig. 5(b)). From the distributions of modes 3 and 4 and the variations of the corresponding POD coefficients, it can be inferred that the disturbances formed by this pair of modes are irregular, and the amplitudes of disturbances are relatively small, so this pair of modes represent the small scale vortical structures.

Fig. 11 gives the energy distribution of POD modes. The first mode occupies 72.6% of the energy, the second mode represents 15.7% of the energy, the third and the fourth modes only represent 3.2% and 2.5% of the energy, respectively. The first two modes together represent 88.3% of the energy, so the spiral rotation of the vortex core dominates the flow in this region, which is in accordance with the observation in Fig. 7(c), in which the peaks at primary pressure fluctuation frequency are strong. Fig. 12(a) shows the original instantaneous pressure field at a time t_0 and Fig. 12(b) shows the corresponding reconstructed pressure field using the first two modes. The comparison of the two fields indicates that the major information of the original pressure field can be given by the reconstructed pressure field. Evolution of the instantaneous reconstructed pressure field using the first two modes in approximately one cycle is shown in Figs. 12(c), (d), (e) and (f), (where $\Delta t = 0.1$ and according to the primary frequency of the first two modes, $4\Delta t$ is approximately one cycle) and the spiral motion of the vortex core can be observed clearly.

Fig. 13 shows the streamlines and velocity magnitude contours of the time-averaged flow field (12,000 time steps are used for averaging the flow field) in four cross-section planes at $\alpha = 36°$. At the cross-section $x/L = 0.2$, there are a pair of primary vortices, which reflect the flow structures of nose vortices. At the cross-section $x/L = 0.4$, there are two pairs of concentrated primary vortices, the inboard one reflects the flow structures of nose vortices and the outboard one reflects the flow structures of strake vortices. At the cross-section $x/L = 0.6$, the nose vortices have disappeared, while for the strake vortices

https://doi.org/10.4208/cicp.OA-2016-0132 Published online by Cambridge University Press

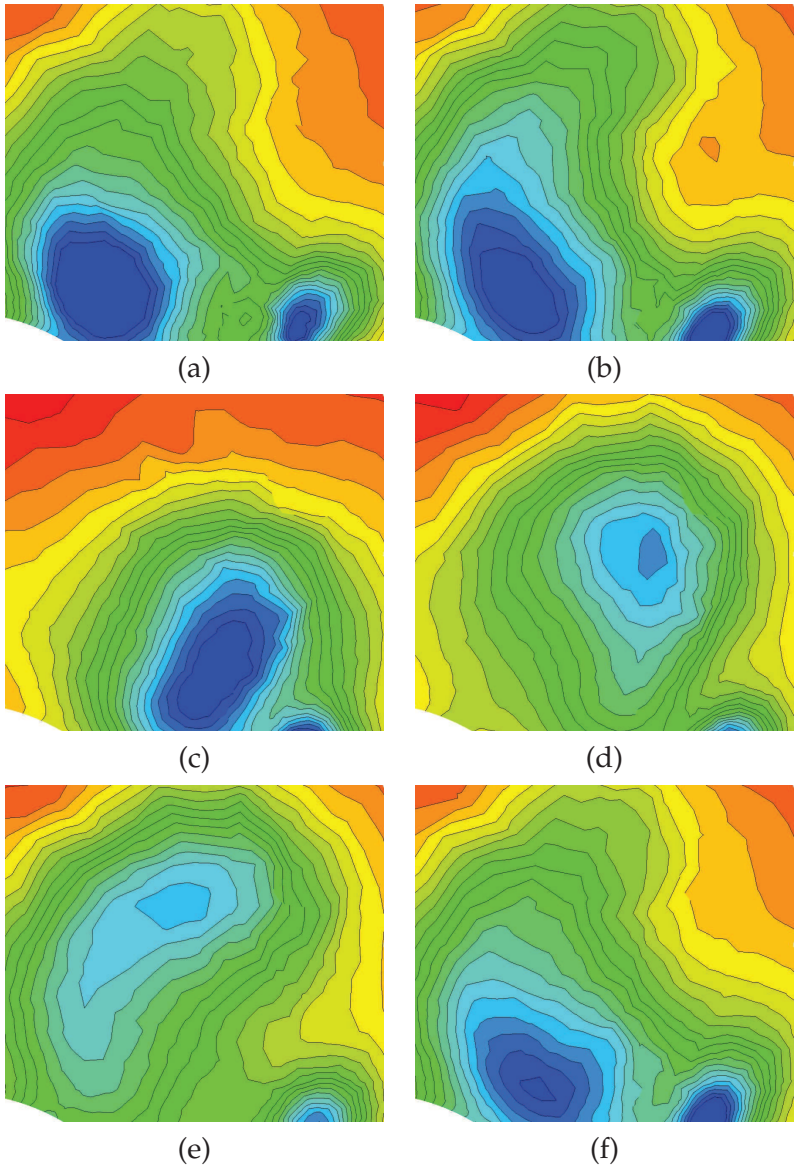


Figure 12: The original pressure field and the reconstructed pressure field using first two modes: (a) Original pressure field at t_0, (b) Reconstructed pressure field at t_0, (c) Reconstructed pressure field at $t_0+\Delta_t$, (d) Reconstructed pressure field at $t_0+2\Delta_t$, (e) Reconstructed pressure field at $t_0+3\Delta_t$, (f) Reconstructed pressure field at $t_0+4\Delta_t$.

the core region broadens remarkably. At the same time, it can be observed that the flow fields near left and right vortex core regions are almost symmetrical, which indicates that the analysis about the spiral motions of left and right vortex cores mentioned previously is reasonable. At the cross-section $x/L=0.8$, the strake vortices corresponding to SST-

https://doi.org/10.4208/cicp.OA-2016-0132 Published online by Cambridge University Press

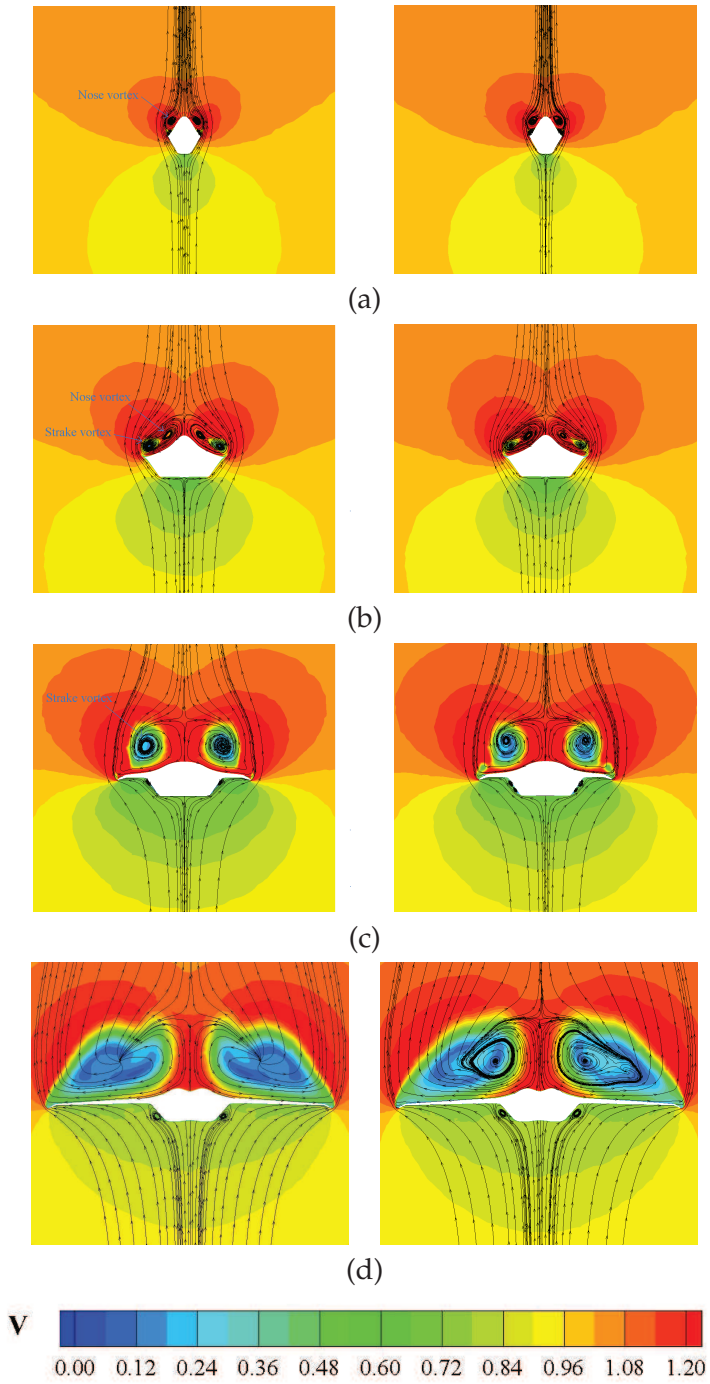


Figure 13: Streamlines and velocity magnitude contours of the time-averaged flow field at α=36°: SST-URANS solution (left) and SST-IDDES solution (right) (a) x/L=0.2, (b) x/L=0.4, (c) x/L=0.6, (d) x/L=0.8, Legend: Velocity magnitude.

https://doi.org/10.4208/cicp.OA-2016-0132 Published online by Cambridge University Press

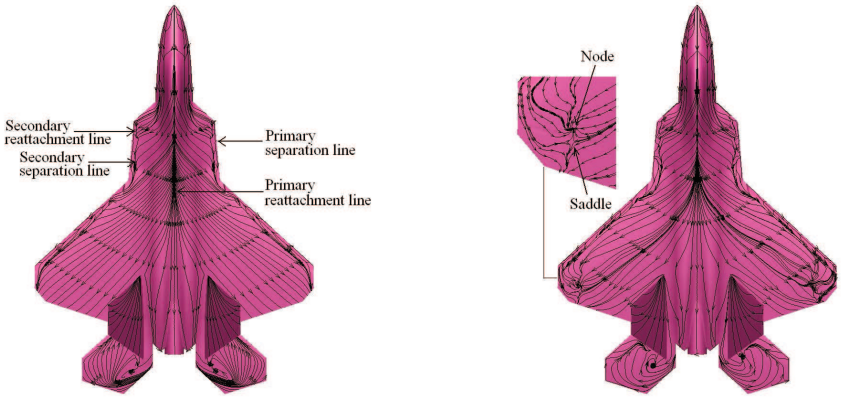
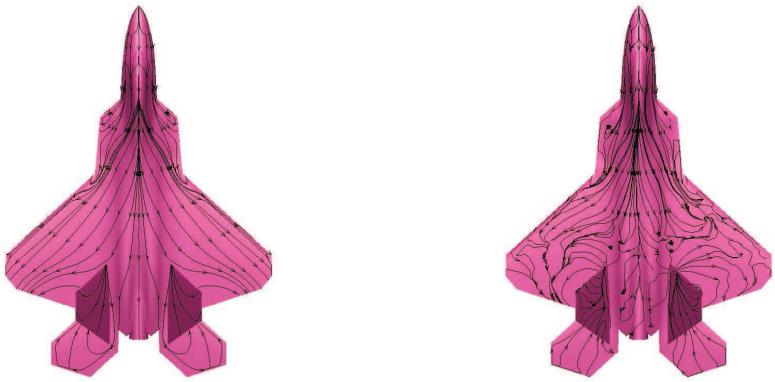


Figure 14: Flow topology for the aircraft model at $\alpha=36^\circ$, (a) SST-URANS solution, (b) SST-IDDES solution.

URANS solution have disappeared, meanwhile the strake vortices corresponding to SST-IDDES solution are still visible, the flow field is in the early stages of vortex breakdown, and the flow structures are slightly asymmetrical (maybe with more time steps used for averaging the flow structures will be symmetrical, but this is quite expensive and time consuming). In the cross sections $x/L=0.4$, $x/L=0.6$, $x/L=0.8$, it can be found that induced by the primary vortices, the flow reattaches on the upper surface of the aircraft model near the symmetrical plane, and separates from the upper surface at the outer edge of the model.

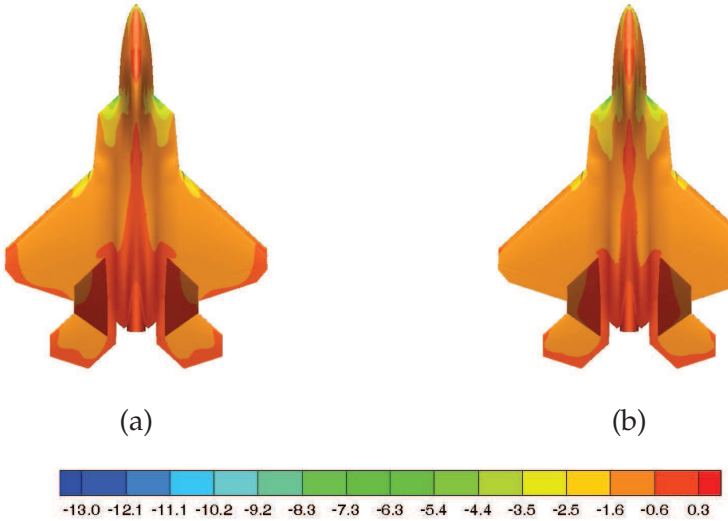
To show more details about the computed separation and reattachment patterns, Fig. 14 gives the flow topology on the upper surface of the aircraft model. The primary separation line is fixed at the outer leading edge. The primary reattachment line is located at the center line of the aircraft model. The secondary separation line is located close to the outer leading edge of the model, and is also clearly visible. The secondary reattachment line is located between the primary separation line and the secondary separation line, and very close to the primary separation line, so this line can not be observed clearly. It is clearly shown that in most region of the upper surface of the wing, the flow remains attached, though the aircraft model is at a high incidence angle, so higher lift and larger stall angle can be obtained with the use of delta, double delta or diamond wings. However, for the SST-IDDES solution flow separation has taken place at the tip of the upper surface of the wing, and meanwhile at the strake the secondary separation line is more inboard and the secondary separation region is wider, compared with the SST-URANS results. Therefore, a conclusion can be drawn that a larger flow separation region is predicted by the SST-IDDES solution. To support this argument, the flow topology on the upper surface of the aircraft model in a deep stall is also presented in Fig. 15 at $\alpha=50^\circ$, and from the separation and reattachment patterns it is not difficult to obtain the same

https://doi.org/10.4208/cicp.OA-2016-0132 Published online by Cambridge University Press



(a) (b)

Figure 15: Flow topology for the aircraft model at $\alpha=50^\circ$, (a) SST-URANS solution, (b) SST-IDDES solution.



(a) (b)

Figure 16: Time averaged surface pressure coefficient contours at $\alpha=36^\circ$, (a) SST-URANS solution, (b) SST-IDDES solution, Legend: C_p.

conclusion. This brings somewhat a surprise, why the SST-IDDES solution gives higher lift at the same flow conditions? To explain this phenomenon, comparison of the surface pressure coefficients for the two numerical solutions are provided in the following paragraph.

Fig. 16 shows the time averaged surface pressure coefficient contours of the two numerical flow fields at $\alpha=36^\circ$. From this figure, it can be found that the SST-URANS solution shows a faster pressure recovery on the leeward side of the aircraft. To give

https://doi.org/10.4208/cicp.OA-2016-0132 Published online by Cambridge University Press

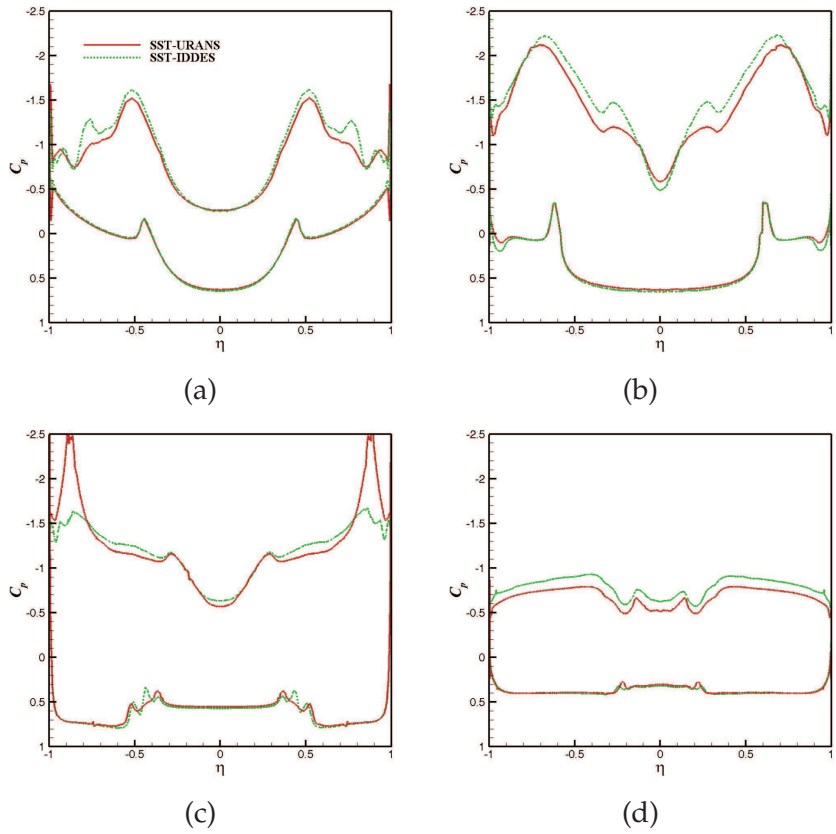


Figure 17: Comparison of surface pressure coefficients at $\alpha=36°$, (a) $x/L=0.2$, (b) $x/L=0.4$, (c) $x/L=0.6$, (d) $x/L=0.8$.

more details about the differences in pressure distributions, Fig. 17 shows a comparison of the computed pressure coefficient at four stations ($x/L=0.2,0.4,0.6,0.8$). On the upwind surface of the aircraft model, the differences in pressure coefficient distributions are very small and only can be found near the corners of the fuselage (as shown in Fig. 17(b) and Fig. 17(c)). The possible reason for the differences near corners is that in these regions flow separation has taken place (as shown in Fig. 13(c) and Fig. 13(d)) and DES performs in LES mode, so the differences become a little visible. On the leeward surface of the aircraft model, the differences of pressure distributions are clearly visible, because of the complex vortex flows and consequently wider LES mode regions in DES. At $x/L=0.2$, the primary suction peak reflects the effect of nose vortex, and it can be observed that with the IDDES solution higher suction peak is obtained, and the corresponding secondary suction peak and tertiary suction peak are also visible. At $x/L=0.4$, the suction peak related to nose vortex is reduced, especially for the SST-URANS solution, and the primary suction peak reflects the effect of strake vortex, it can also be found that with the IDDES solution higher suction peak is obtained. At $x/L=0.6$, the suction peak related to strake

https://doi.org/10.4208/cicp.OA-2016-0132 Published online by Cambridge University Press

vortex decays significantly due to the vortex core moving away from the upper surface and the core region expanding remarkably (as shown in Fig. 13(c)), which weakens the influence of strake vortex on surface pressure distribution, meanwhile the primary suction peak is located close to the outer leading edge of the wing, which is mainly due to the influence of the shear layer formed along the leading edge of the wing, and the primary suction peak corresponding to SST-URANS solution is significantly high, which may be related to the more compact two dimensional shear layer of URANS solution (From Fig. 13(c), it can be observed that near the outer edge of the wing the SST-URANS solution displays larger streamline curvature and higher velocity gradient). At $x/L=0.8$, the pressure coefficient distributions become relatively flat, the pressure recovery on the upper surface of the aircraft model is significant (from Fig. 13(d) it can be observed that near the upper surface of the aircraft model the velocity magnitudes become relatively low), and meanwhile the SST-IDDES solution shows lower pressure coefficients, though flow separation has taken place at this station for the SST-IDDES solution. From the above comparison, it can be concluded that although separation regions predicted by IDDES simulation are larger than those by URANS at the same aerodynamic conditions (flow separation is usually accompanied by pressure recovery), the corresponding pressure difference between the upper and lower surface predicted by IDDES simulation is still larger, so higher lift can be obtained by IDDES simulation.

4 Conclusions

In this paper, the unstructured/hybrid grid based second order hybrid scheme is applied to DES simulations of a complex modern fighter model. From the comparisons of numerical results and experimental data, the method presented in this paper is obviously superior to the traditional (U)RANS method. The vortex breakdown phenomenon is clearly visible in the unsteady DES flow field and it is found that the broken vortex structures may cause structural vibrations and mechanical fatigue of vertical tails. The correlation coefficient analysis about the DES flow field indicates that the motion of the primary vortex in axial direction is highly nonlinear and the instantaneous flow field is not mirrored about the symmetric plane. The possible reason for non-symmetry is due to the phase difference between left and right vortex motions according to the PSD analysis, so it can be observed that the corresponding time-averaged flow field is almost mirrored. The POD analysis about the DES flow field indicates that the first two modes of POD represent the spiral rotation of the vortex structure, and occupy most of the energy. In the comparison of results for separation and reattachment patterns computed by DES and (U)RANS, we find that the higher and more accurate lift obtained by DES simulation is owing to the larger pressure difference between the upper and lower surfaces predicted by this method, and meanwhile the separation regions predicted by DES simulation are even larger. These numerical results have demonstrated the capability of present DES solver for industrial applications. In the future, the grid-adaptive technique

https://doi.org/10.4208/cicp.OA-2016-0132 Published online by Cambridge University Press

will be coupled into the simulations to improve the resolution of complex turbulence flow structures. Furthermore, the dynamic aerodynamic performance of maneuvering aircraft will be carried out based on moving grid.

Acknowledgments

This work is supported by the National Natural Science Foundation of China (Grant No. 11532016 and No. 91530325) and National Key Research and Development Program (No. 2016YFB0200701).

References

[1] P. R. Spalart, Strategies for turbulence modelling and simulations, Int. J. Heat Fluid Flow, 21 (2000), 252–263.
[2] P. R. Spalart and S. R. Allmaras, A one-equation turbulence model for aerodynamic flows, AIAA paper 92-0439, 1992.
[3] Z. Jiang, Z. L. Xiao and Y. P. Shi et al., Constrained large-eddy simulation of wall-bounded compressible turbulent flows, Phys. Fluids, 25(106102) (2013), 1–28.
[4] H. Li and S. H. Zhang, Direct numerical simulation of decaying compressible isotropic turbulence, Chinese J. Theoret. Appl. Mech., 44(4) (2012), 673–686.
[5] J. Fröhlich, D. von Terzi, Hybrid LES/RANS methods for the simulation of turbulent flows, Process Aerospace Sci., 44 (2008), 349–377.
[6] P. R. Spalart, W. H. Jou and M. Strelets et al., Comments on the feasibility of LES for wings and on a hybrid RANS/LES approach, Proceedings of 1st AFOSR International Conference on DNS/LES, Greyden Press, Columbus, 1997.
[7] M. Strelets, Detached eddy simulation of massively separated flows, AIAA paper 2001-0879, 2001.
[8] R. Mittal and P. Moin, Suitability of upwind-biased finite difference schemes for large-eddy simulation of turbulent flows, AIAA J., 35(8) (1997), 1415–1417.
[9] T. T. Bui, A parallel, finite-volume algorithm for large-eddy simulation of turbulent flow, Comput. Fluids, 29(8) (2000), 877–915.
[10] A. Travin, M. Shur and M. Strelets et al., Physical and numerical upgrades in the detached-eddy simulation of complex turbulent flows, Advances in LES of Complex Flows, Springer-Verlag, Berlin, Heidelberg, 2004.
[11] L. H. Xiao, Z. X. Xiao and Z. W. Duan et al., Improved-Delayed-Detached-Eddy simulation of cavity-Induced transition in hypersonic boundary layer, Proceedings of The Eighth International Conference on Computational Fluid Dynamics, ICCFD8-2014-0247, pp. 1055–1073, Chengdu, China, 2014.
[12] X. B. Deng, X. H. Zhao and W. Yang et al., Dynamic adaptive upwind method and its applications in RANS/LES hybrid simulations, Proceedings of The Eighth International Conference on Computational Fluid dynamics, ICCFD8-2014-0164, pp. 807–814, Chengdu, China, 2014.
[13] T. J. Baker, Mesh generation: Art or Science?, Progress Aerospace Sci., 41(1) (2005), 29–63.
[14] Z. Z. Li, X. J. Yu and J. Zhu et al., A Runge Kutta discontinuous Galerkin method for Lagrangian compressible Euler equations in two-dimensions, Commun. Comput. Phys., 15(4) (2014), 1184–1206.

https://doi.org/10.4208/cicp.OA-2016-0132 Published online by Cambridge University Press

[15] L. P. Zhang, W. Liu and L. X. He et al., A class of hybrid DG/FV methods for conservation laws I: Basic formulation and one-dimensional systems, J. Comput. Phys., 231(4) (2012), 1081–1103.
[16] L. P. Zhang, W. Liu and L. X. He et al., A class of hybrid DG/FV methods for conservation laws II: Two-dimensional cases, J. Comput. Phys., 231(4) (2012), 1104–1120..
[17] L. P. Zhang, W. Liu and L. X. He et al., A class of hybrid DG/FV methods for conservation laws III: Two-dimensional Euler equations, Commun. Comput. Phys., 12(1) (2012), 284–314.
[18] Z. J. Wang, Spectral (finite) volume method for conservation laws on unstructured grids I: basic formulation, J. Comput. Phys., 178(2) (2002), 210–251.
[19] Z. J. Wang and Y. Liu, The spectral difference method for the 2D Euler equations on unstructured grids, AIAA paper 2005-5112, 2005.
[20] H. T. Huynh, A reconstruction approach to high-order schemes including discontinuous Galerkin for diffusion, AIAA paper 2009-403, 2009.
[21] Y. Zhang, L. P. Zhang, X. He and X. G. Deng, Detached eddy simulation based on unstructured and hybrid grid, Chinese Journal of Aeronautics, 36(9) (2015), 2900–2910.
[22] Y. Zhang, L. P. Zhang, X. He and X. G. Deng, An improved second-order finite-volume algorithm for detached-eddy simulation based on hybrid grids, Commun. Comput. Phys., 20(2) (2016), 459–485.
[23] F. Menter, Zonal two-equation k-ω turbulence models for aerodynamic flows, AIAA paper 93-2906, 1993.
[24] M. S. Gritskevich, A. V. Garbaruk and J. Schütze et al., Development of DDES and IDDES formulations for the k-ω shear stress transport model, Flow Turbul. Combust., 88(3) (2012), 431–449.
[25] E. Sozer, C. Brehm and C. C. Kiris, Gradient calculation methods on arbitrary polyhedral unstructured meshes for cell-centered CFD solvers, AIAA paper 2014-1440, 2014.
[26] P. L. Roe, Approximate Riemann solvers, parameter vectors, and difference schemes, J. Comput. Phys., 43 (1981), 357–372.
[27] L. P. Zhang and Z. J. Wang, A block LU-SGS implicit dual time-stepping algorithm for hybrid dynamic meshes, Comput. Fluids, 33(7) (2004), 891–916.
[28] X. He, L. P. Zhang and Z. Zhao et al., Research and development of structured/unstructured hybrid CFD software, Transactions of Nanjing University of Aeronautics & Astronautics, 30(S) (2013), 116–120.
[29] X. He, L. P. Zhang and Z. Zhao et al., Validation of HyperFLOW in subsonic and transonic flow, Acta Aerodynamica Sinica, 34(2) (2016), 267–275.
[30] J. Liu, H. S. Sun, Y. Huang, Y. Jiang and Z. X. Xiao, Numerical investigation of an advanced aircraft model during pitching motion at high incidence, Sci. China Tech. Sci., 59(2) (2016), 276–288.
[31] F. M. Payne, T. T. Ng and R. C. Nelson, Visualization and flow surveys of the leading edge vortex structure on delta wing platforms, AIAA paper 86-0330, 1986.
[32] K. E. Meyer, J. M. Pedersen, and O. Özcan, A turbulent jet in crossflow analysed with proper orthogonal decomposition, J. Fluid Mech., 583 (2007), 199–227.

https://doi.org/10.4208/cicp.OA-2016-0132 Published online by Cambridge University Press